

# An empirical model of the global distribution of plasmaspheric hiss based on Van Allen Probes EMFISIS measurements

JingZhi Wang<sup>1</sup>, Qi Zhu<sup>1</sup>, XuDong Gu<sup>1\*</sup>, Song Fu<sup>1\*</sup>, JianGuang Guo<sup>2</sup>, XiaoXin Zhang<sup>2</sup>, Juan Yi<sup>1</sup>, YingJie Guo<sup>1</sup>, BinBin Ni<sup>1</sup>, and Zheng Xiang<sup>1</sup>

<sup>1</sup>Department of Space Physics, School of Electronic Information, Wuhan University, Wuhan 430079, China;

<sup>2</sup>Key Laboratory of Space Weather, National Center for Space Weather, China Meteorological Administration, Beijing 100081, China

## Key Points:

- The empirical model is a third-order polynomial function of  $L$ -shell, magnetic local time (MLT), magnetic latitude (MLAT), and  $AE^*$
- The model can perform the hiss amplitude distribution by  $L/MLT$  and  $L/MLAT$
- All data are based on Van Allen Probes EMFISIS measurements

**Citation:** Wang, J. Z., Zhu, Q., Gu, X. D., Fu, S., Guo, J. G., Zhang, X. X., Yi, J., Guo, Y. J., Ni, B. B., and Xiang, Z. (2020). An empirical model of the global distribution of plasmaspheric hiss based on Van Allen Probes EMFISIS measurements. *Earth Planet. Phys.*, 4(3), 246–265. <http://doi.org/10.26464/epp2020034>

**Abstract:** Using wave measurements from the EMFISIS instrument onboard Van Allen Probes, we investigate statistically the spatial distributions of the intensity of plasmaspheric hiss waves. To reproduce these empirical results, we establish a fitting model that is a third-order polynomial function of  $L$ -shell, magnetic local time (MLT), magnetic latitude (MLAT), and  $AE^*$ . Quantitative comparisons indicate that the model's fitting functions can reflect favorably the major empirical features of the global distribution of hiss wave intensity, including substorm dependence and the MLT asymmetry. Our results therefore provide a useful analytic model that can be readily employed in future simulations of global radiation belt electron dynamics under the impact of plasmaspheric hiss waves in geospace.

**Keywords:** hiss; Van Allen Probes; global model

## 1. Introduction

Plasmaspheric hiss is a broadband incoherent whistler mode emission with frequencies ranging from  $\sim 20$  Hz to  $\sim 2$  kHz that is observed predominantly inside the plasmasphere or high density plumes (Thorne et al., 1973, 1979; Meredith et al., 2004; Li W et al., 2013, 2015a, b; Ni BB et al., 2014; Shi R et al., 2017). It can persist under quiet conditions; its fluctuations are positively correlated with the level of solar activity (Smith et al., 1974; Thorne et al., 1973, 1974). Broadband amplitudes of plasmaspheric hiss range from a few pT to as high as 100 pT (Thorne et al., 1973; Smith et al., 1974; Meredith et al., 2004). Plasmaspheric hiss is mainly observed at a broad range of wave normal angle, e.g., its propagation near the geomagnetic equator is predominantly field-aligned, but oblique at higher latitudes (Santolík et al., 2001; Bortnik et al., 2008).

It has been well recognized that electron scattering by plasmaspheric hiss acts as a dominant contributor to formation of the slot region, which separates the radiation belts into inner ( $1.2 < L < 2$ ) and outer ( $3 < L < 7$ ) parts (Lyons et al., 1972; Lyons

and Thorne, 1973; Albert, 1994; Abel and Thorne, 1998a, b; Meredith et al., 2004, 2006a, b). Resonant interactions with plasmaspheric hiss result in electron scattering losses with decay time scales varying from less than 1 hour to tens or hundreds of days. Decay times are closely dependent on electron energy, ambient magnetic field, and plasma density, as well as on wave amplitude, spectral intensity, and wave normal angle (WNA) distribution of the hiss waves as a function of spatial location and geomagnetic activity level (Meredith et al., 2007; Ni BB et al., 2014; Yu J et al., 2017). As reported in Summers et al. (2007a, b), the pitch angle diffusion coefficient of resonant electrons in quasi-linear formalisms is proportional to the wave amplitude. Thus, the development of a reliable global model of hiss wave amplitude is essential to facilitate quantification of hiss-induced electron scattering rates and resultant global variations of radiation belt electron distribution.

A number of empirical models of hiss wave global distribution have been constructed in previous studies (Meredith et al., 2004; Kim et al., 2015; Li et al., 2015b). Data from the Combined Release and Radiation Effect Satellite (CRRES) are utilized to investigate the features of plasma waves. Meredith et al. (2004) presented elaborate global maps of hiss wave intensity and described its distribution features. Orlova et al. (2014) produced empirical quadratic fittings of  $B_w^2$  as a function of  $K_p$ ,  $L$ , and geomagnetic latitude ( $\lambda$ ) for the daytime and nighttime sectors respectively. However,

Correspondence to: X. D. Gu, guxudong@whu.edu.cn

S. Fu, fusion@whu.edu.cn

Received 20 JAN 2020; Accepted 02 MAR 2020.

Accepted article online 08 MAY 2020.

©2020 by Earth and Planetary Physics.

the CRRES wave instrument has limitations in space and frequency band, in particular it records only electric field data; accordingly, some important wave information such as magnetic field spectral intensity was estimated, based on theoretical assumptions. Characteristics of whistler mode waves have also been analyzed by Agapitov et al. (2013) with Cluster data, which separate chorus from hiss merely by  $f_{ce}$  (the electron cyclotron frequency), i.e., chorus frequency above  $0.1f_{ce}$  and hiss below  $0.1f_{ce}$ , though their frequencies may actually overlap. Subsequently Agapitov et al. (2014) parameterized the hiss wave activity at  $L < 2$  based on Akebono spacecraft observations. In addition, combined observations of Cluster (Agapitov et al., 2013) and Polar (Tsurutani et al., 2015) showed that hiss can be widely distributed over the magnetic latitude, extending to  $\lambda > 45^\circ$ .

Recently, using data from Van Allen Probes, Spasojevic et al. (2015) and Yu J et al. (2017) constructed one-dimensional fitting models of hiss wave amplitude as a function of  $AE$ ,  $L$ , MLT, and  $K_p$ ,  $L$ , MLT, respectively. Highlighting the dependence of hiss amplitude on single variables, those studies focus on the fluctuations of the fitting curves associated with each variable in their hypothetical formulae and do not reproduce the observed latitudinal variations of hiss wave amplitude. Since the dependence on MLAT cannot be neglected in accurate predictions of hiss amplitude, as previous studies have done, the present investigation considers the combined effects of  $L$ , MLT, MLAT, and  $AE^*$ , and intends to establish a more comprehensive empirical model of plasmaspheric hiss amplitude as a function of these four input parameters.

## 2. Data and Methodology

Van Allen Probes were launched on September 8, 2012 with perigee of  $\sim 1.1R_E$  (radius of the Earth), apogee of  $\sim 5.8R_E$ , inclination of  $10^\circ$ , and an orbital period of  $\sim 9$  hours. Equipped with identical electromagnetic detectors, the EMFISIS instruments onboard Van Allen Probes can acquire high quality measurement of whistler-mode waves in the inner magnetosphere (Kletzing et al., 2013). The waveform receiver (WFR) on EMFISIS provides wave power spectral densities ranging from 10 Hz–12 kHz with a temporal resolution of 6 s. The high frequency receiver (HFR) records electric spectral information between 10 and 400 kHz, in which the traces of upper hybrid resonance (UHR) frequency can be used to estimate the ambient plasma density (Mosier et al., 1973) and identify the location of the plasmapause that separates the regions outside and inside the plasmasphere (e.g., He F et al., 2011, 2013, 2016, 2017; Katus et al., 2015; Verbanac et al., 2015; Zhang XX et al., 2017a, b).

According to the wave characteristics of hiss emissions, in this study we identify a hiss event with the ellipticity  $> 0.7$  (i.e., right-hand polarized) and the frequency band within 10–2000 Hz in the

plasmasphere. By doing so, we distinguish the hiss waves from chorus waves outside the plasmasphere and from magnetosonic waves with nearly linear polarization. Subsequently, we integrate the wave spectral intensity in the determined frequency band to calculate the wave amplitude ( $B_w$ ). In our following analysis we concentrate on the hiss emissions with  $B_w \geq 5$  pT.

The adopted database consists of observations made during the period from September 8, 2012 to June 30, 2017:  $L$ -shell ( $L$ ), magnetic local time (MLT), magnetic latitude (MLAT),  $AE^*$  (averaged value of the  $AE$  index in the previous hour), and hiss wave amplitude ( $B_w$ ) with temporal resolution of 6 s. We then implement two methods to construct our empirical global model of hiss wave amplitude. In each method, we divide the entire database data into two groups, i.e., the training group and the test group. The training group is used as the baseline to obtain the fitting coefficients in the regression, while the test group is regarded as a comparison to examine the model's performance and verify its reliability.

As tabulated in Table 1, for Method #1, data in first three years are selected as the training group (Database 1) and the remaining datasets are reserved as the test group (Database 2). For Method #2, we divide them in another way: data collected during odd-number days are set as the training group (Database 3), and the others are the test group (Database 4). Furthermore, we divide each Database (1–4) into 12 sub-groups in terms of  $AE^*$  and MLT, to take into account the geomagnetic effect and MLT variation. Hence, we rank the  $AE^*$  values into three geomagnetic levels (quiet,  $AE^* < 100$  nT; moderate,  $100 \text{ nT} \leq AE^* \leq 300$  nT; active,  $AE^* > 300$  nT) and classify all the MLTs into four sectors (dayside, 09–15; duskside, 15–21; nightside, 21–03; dawnside, 03–09). Correspondingly, twelve groups of fitted parameters need to be derived from regression of these training groups, and we then examine the feasibility of the resulting fitting functions through self-consistency and verification with the test groups. To check differences between the model and observations, we define the variable,  $R_d$ , given as  $\frac{|w_{\text{obs}} - w_{\text{mod}}|}{w_{\text{obs}}}$ , where  $w_{\text{obs}}$  is the observed hiss wave amplitude and  $w_{\text{mod}}$  is the model result, as a criterion to evaluate our empirical model. Clearly, lower values of  $R_d$  represent higher similarity between observations and the model.

Taking  $L$ , MLT, MLAT,  $AE^*$ , and  $B_w$  as known quantities and  $F(i, j, k, l)$  as unknown, we implement the fits of a third-order polynomial function as follows:

$$\log_{10}(B_w) = \sum_{i=0}^3 \sum_{j=0}^2 \sum_{k=0}^2 \sum_{l=0}^2 F(i, j, k, l) A^i B^j C^k D^l, \quad (1)$$

where the parameters  $A$ ,  $B$ ,  $C$ , and  $D$  are quantified as  $L/10$ ,  $MLT/24$ ,  $MLAT/20$ , and  $AE^*/500$ , respectively. Following previous studies of Spasojevic et al. (2015) and Yu et al., (2017), we set the

**Table 1.** Classification of each adopted database.

Type	Method #1	Method #2
Training group	Every day during the period of 2012/9/8–2015/9/8 (Database 1)	Odd-number days during the period of 2012/9/8–2017/6/30 (Database 3)
Test group	Every day during the period of 2015/9/9–2017/6/30 (Database 2)	Even-number days during the period of 2012/9/8–2017/6/30 (Database 4)

maximum values of  $i$ ,  $j$ ,  $k$ , and  $l$  as 3, 2, 2, and 2, respectively; consequently we have 108 coefficients for the fit to each training group.

### 3. Analysis Results

Based on the two methods described above, we do the fits for the training groups, compute the model results with the obtained polynomial fitting functions, and perform quantitative comparisons with the statistical observations of the test groups.

First, we follow Method #1 to establish the empirically analytic model of plasmaspheric hiss intensity, the results of which are shown in Figures 1–4. Figures 1 and 2 show the global distributions of time-averaged root-mean-square (RMS) hiss wave am-

plitudes in the equatorial plane and the meridian plane, at resolution of  $0.5L \times 1\text{MLT}$  and  $1^\circ \times 0.1L$ , respectively, obtained using Database 1 (the period from 2012/9/8–2015/9/8), and comparisons between these statistical observations and results of the empirical model.

The first-row subplots in Figure 1 reveal that the hiss wave amplitude strengthens significantly when  $AE^*$  increases and that the waves on the dayside are much stronger than those at the nightside. Overall, hiss wave activity shows a strong dependence on  $L$ -shell, MLT, and geomagnetic level. Correspondingly, the second-row panels illustrate model results of hiss wave amplitude for the same time period as in Figures 1a–1c, obtained using the fitted three-order polynomial function (i.e., Equation (1)). It is evident

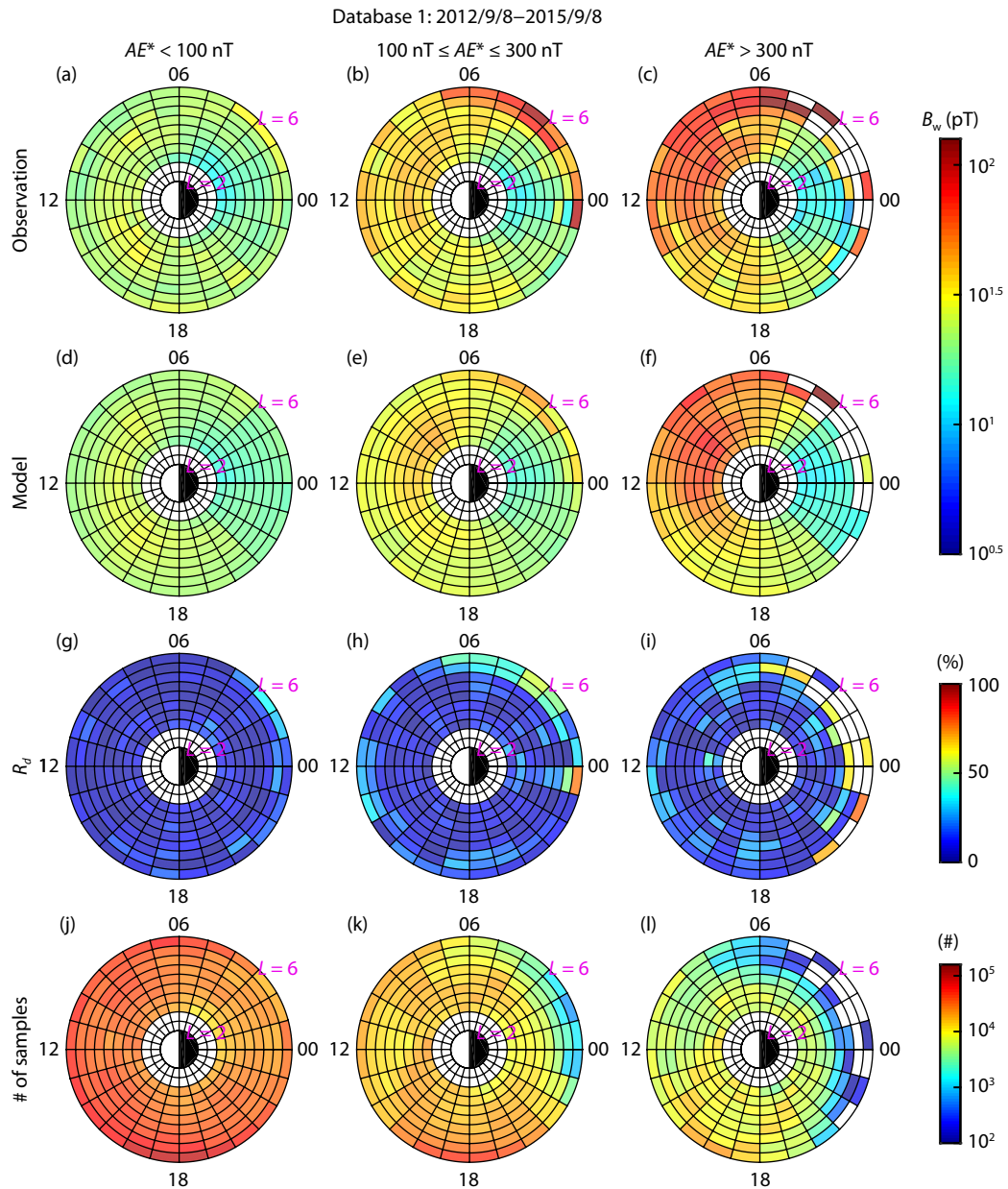


**Figure 1.** (a–c) Global  $L$ -MLT distribution of hiss wave amplitude from Van Allen Probe observations of Database 1; (d–f) self-consistent model results of Database 1; (g–i) relative differences ( $R_d$ ) between them; (j–l) corresponding numbers of samples collected during quiet, moderate, and active times (left to right).

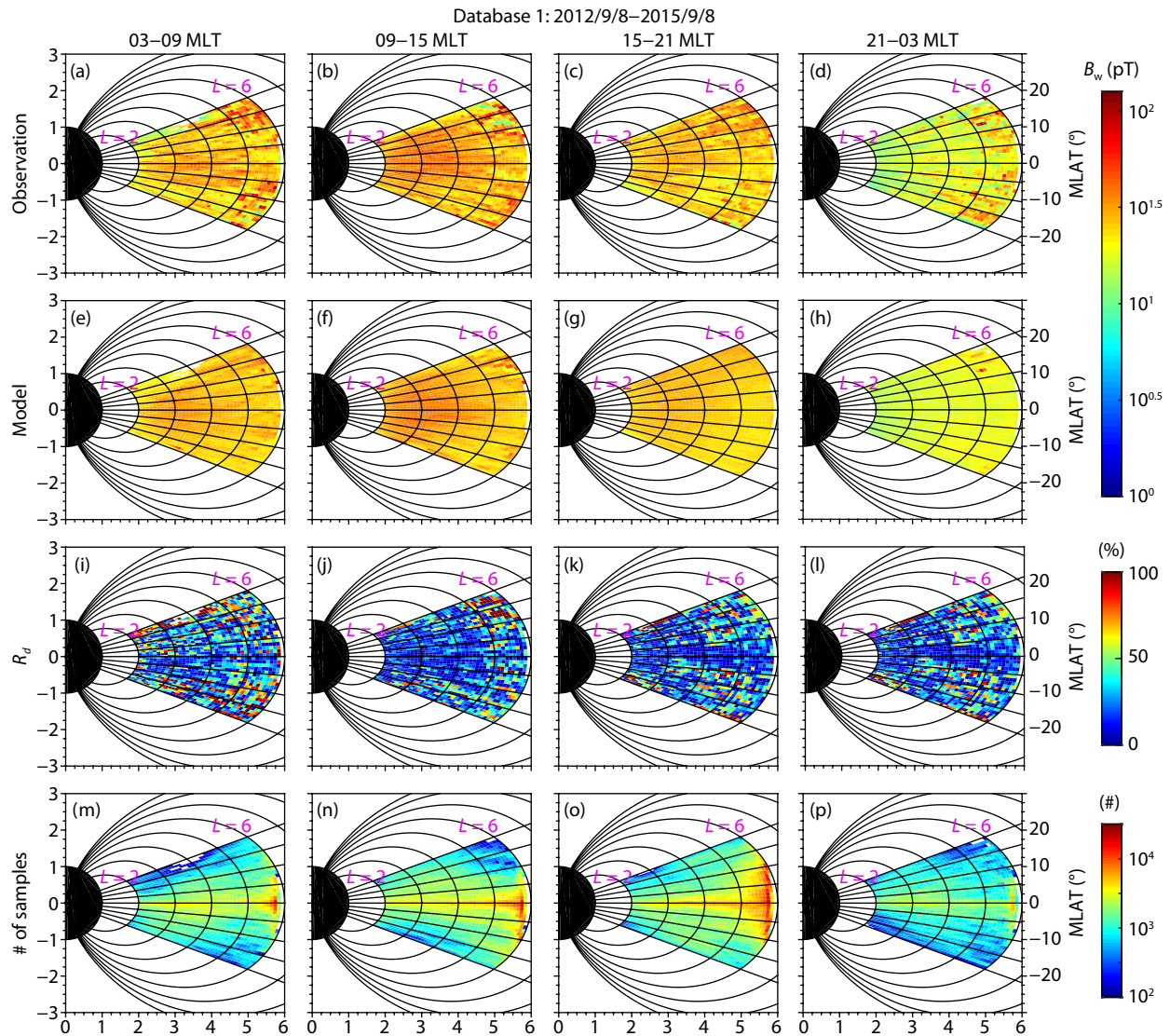


**Figure 2.** (a–d) Latitudinal  $L$ -MLAT distribution of hiss wave amplitude from observations in Database 1; (e–h) self-consistent model results of Database 1; (i–l) relative differences ( $R_d$ ) between them; (m–p) corresponding numbers of samples during different MLT sectors (left to right).

that the fitted function reflects the major features of the observed global dynamics of plasmaspheric hiss. The relative differences ( $R_d$ ) between the observations and model results are shown in Figures 1g–1i. It is clearly seen that during most bins the relative differences are less than 15%, though the differences are larger in some limited regions of  $L = 4.5\text{--}6$  and  $\text{MLT} \sim 23\text{--}06$ .

Figure 2 results are similar to those in Figure 1 but as a function of  $L$  and MLAT in the indicated four MLT sectors. It can be seen clearly that, besides its  $L$ -shell and MLT dependence, the hiss wave amplitude also depends on MLAT but in a less significant manner. Figures 2i–2l confirm that during most bins the relative differences between the observations and model results are less than 20%, showing good agreement between model and empirical data.

Figures 3–4 present Database 2 (the test data) results in the same format as Figures 1–2, to verify consistent model performance during periods exclusive to the training group.

While the wave observations are slightly different from those in

Database 1, the dominant trends are favorably similar. In order to validate the feasibility of the fitting function, we compare the observations from Database 2 (Figures 3a–3c) with the model results for the same period that are obtained using the empirically analytic function model as a function of  $L$ , MLT, MLAT, and  $AE^*$  derived using Database 1 (Figures 3d–3f). Apparently, large differences between the observational and model results occur especially during geomagnetically moderate and active times, showing that the value of  $R_d$  can be well above 1 in association with large deviation of the model results from the observations. In addition, it is distinct in Figure 4 that the model results become much less reliable compared to the observations, especially for the interval of  $\text{MLT} = 03\text{--}09$ . These discrepancies between model results and observations during the time period exclusive to the test group tell that the empirical model obtained using Method #1 has limitations that make it unsuited to the task of obtaining a global hiss wave distribution.

Accordingly, we adopt Method #2 to establish an empirical model of the global distributions of hiss intensity; that is, the data during

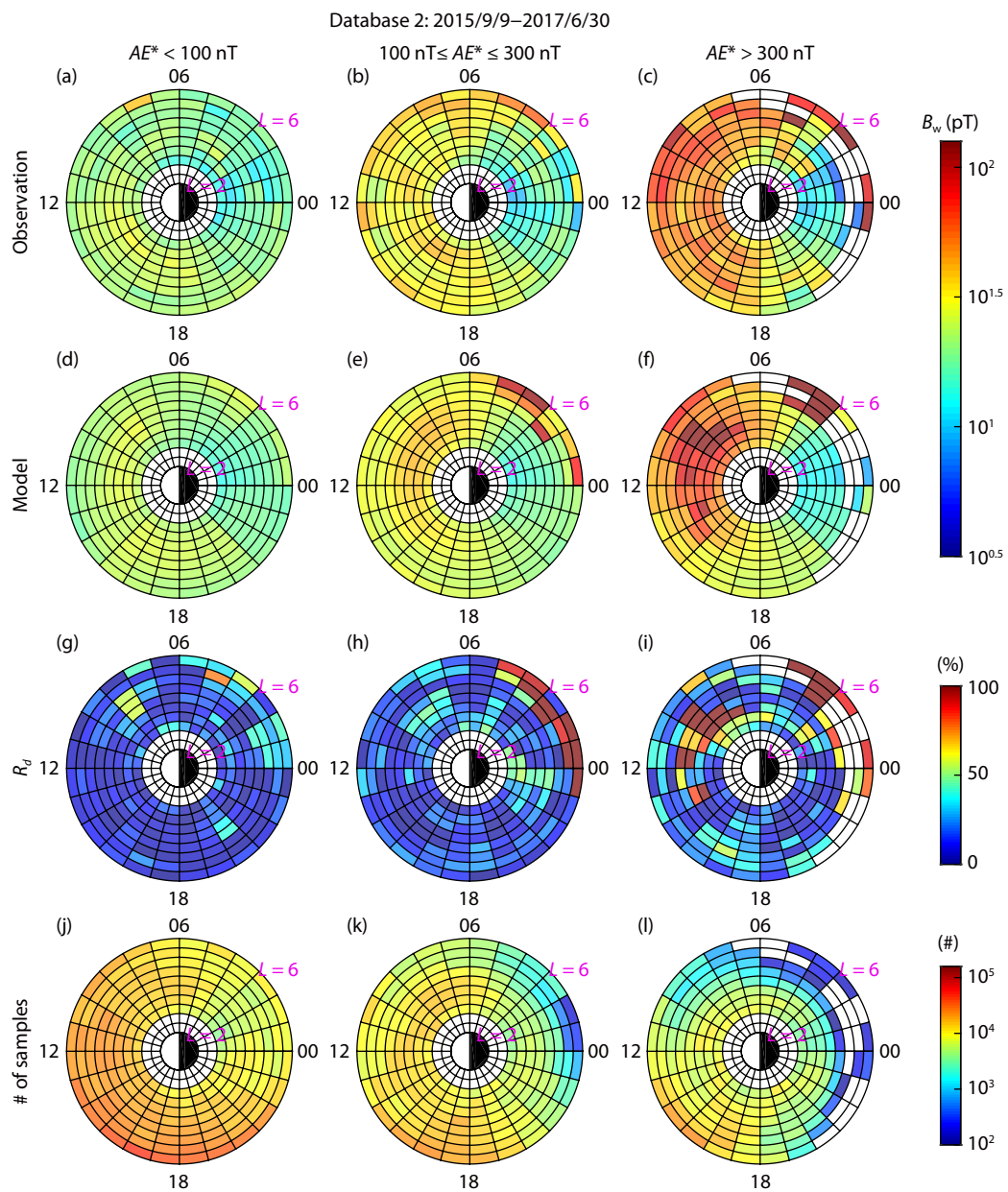


**Figure 3.** (a–c) Global  $L$ -MLT distribution of hiss wave amplitude from observations of Database 2; (d–f) model results calculated by Method #1 of Database 2; (g–i) relative differences ( $R_d$ ) between them; (j–l) corresponding numbers of samples during quiet, moderate, and active times (left to right).

the odd-number days are set as the training group (Database 3) and used to acquire the fitting function  $F(i, j, k, l)$ , and the data during the even-number days are set as the test group to verify the model's performance.

First, we use Database 3 for the fits and self-consistency comparisons, the results of which are shown in Figures 5 and 6. Evidently, the fitting model results and the observations exhibit favorable agreement in most  $L$ -MLT bins (Figure 5), justifying the feasibility of the empirical model. While the differences between the observations and the model become relatively larger in the  $L$ -MLAT bins at high  $L$  shell, the majority of  $R_d$ -values are below ~20% (Figure 6), thereby confirming good performance of the model.

Again, to validate the performance of the fitting model obtained using Database 3 as the training group, we use Database 4 to apply the model and compare the model results with the observations, the results of which are shown in Figures 7 and 8.

Compared with the statistical observations (Figures 7a–7c), the model can reproduce well the global distribution of hiss wave amplitude including the MLT asymmetry and geomagnetic activity dependence (Figures 7d–7f). As shown in Figures 7g–7i, the relative differences ( $R_d$ ) are < 15% for over 80% of  $L$ -MLT bins, justifying good performance of the fitting model, while the model becomes less feasible at high  $L$ -shells on the nightside, especially for active conditions with  $AE^* > 300$  nT. In addition, the empirical model can reproduce well the major features of hiss wave am-

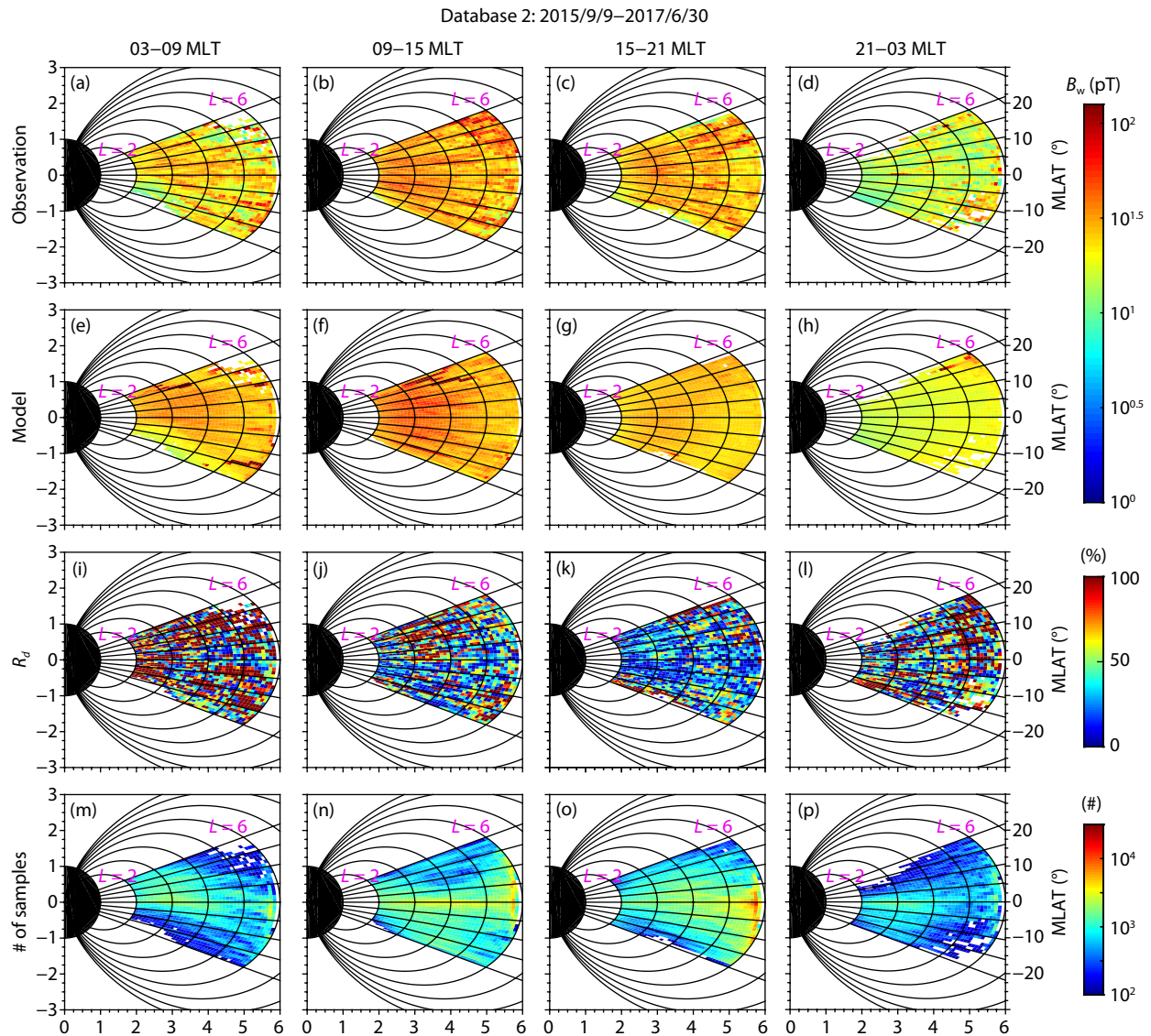


**Figure 4.** (a–d) Latitudinal  $L$ -MLAT distribution of hiss wave amplitude from observations in Database 2; (e–h) model results calculated by Method #1 of Database 2; (i–l) relative differences ( $R_d$ ) between them; (m–p) corresponding numbers of samples during different MLT sectors (left to right).

litude distribution in the  $L$ -MLAT bins for different MLT intervals, as shown by the  $R_d$ -values < 20% in general (Figures 8i–8l).

Some discrepancies at higher latitudes may be attributed to hiss wave amplitude enhancements during geomagnetically disturbed periods, which, however, are difficult to be captured by the fits possible with third-order polynomial functions.

Overall, this study establishes an empirical model of the global distribution of hiss wave intensity by implementing third-order polynomial function fits to the long-term Van Allen Probes EMFISIS wave data, which is determined by Equation (1) and the polynomial coefficients tabulated in Tables S1–S12 in the Appendix for the four considered MLT sectors (i.e., 03–09, 09–15, 15–21, and 21–03) under three geomagnetic conditions (i.e., quiet-time:  $AE^* < 100$  nT; moderate-time:  $100 \text{ nT} \leq AE^* \leq 300$  nT; active-time:  $AE^* > 300$  nT).

#### 4. Concluding Remarks

In the present study, we have used approximately five years of Van Allen Probes EMFISIS wave data to analyze statistically the global distribution of plasmaspheric hiss intensity at  $L = 2$ –6 under various conditions of geomagnetic activity. During quiet times or times of weak substorm activity ( $AE^* < 100$  nT), the hiss wave amplitude distribution is not dependent on MLT. However, when substorm activity intensifies, the hiss wave amplitude distribution is more dependent on MLT and the intense hiss events are concentrated at high  $L$  ( $L > 5$ ) on the morning side and the nightside (MLT  $\sim 00:00$ – $06:00$ ). Furthermore, the observation results (the first row of our Figures 2, 4, 6, and 8) suggest that the hiss amplitude distribution is slightly dependent on MLAT in the data on which the present study is based, which means the distribution is mainly controlled by  $L$  and MLT. The hiss wave amplitude is very intense inside the dayside plasmasphere (the first row of Figures

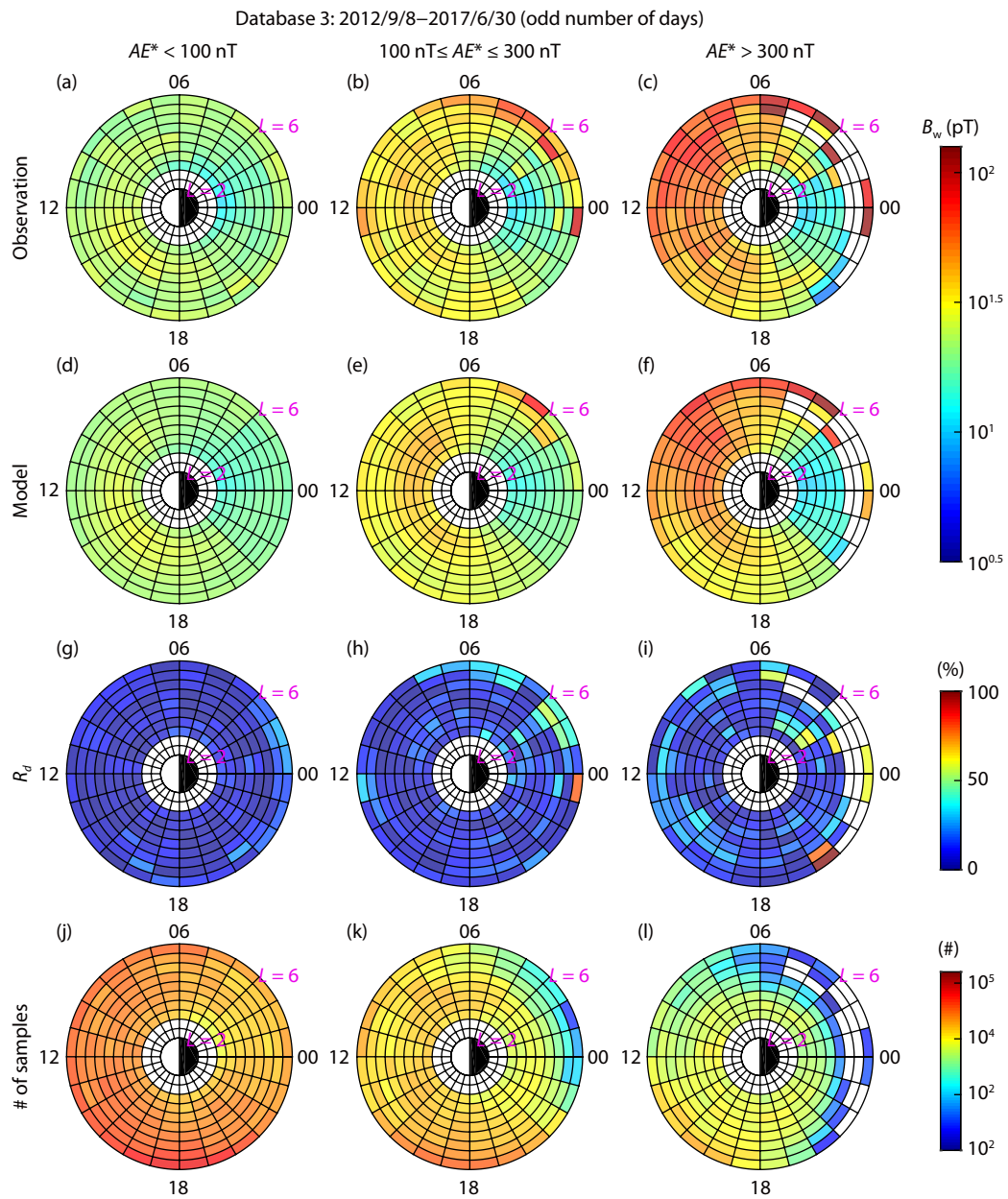


**Figure 5.** (a–c) Global  $L$ -MLT distribution of hiss wave amplitude from observations of Database 3; (d–f) self-consistent model results of Database 3; (g–i) relative differences ( $R_d$ ) between them; (j–l) corresponding numbers of samples collected during quiet, moderate, and active times (left to right).

1, 3, 5, and 7). Inspired by observations that hiss wave amplitudes vary sensitively with spatial location and  $AE^*$ , we have then performed numerical fits to the statistical observations in terms of a third-order polynomial as a function of  $L$ , MLT, MLAT, and  $AE^*$ . By doing so, we have constructed an empirically analytic model of the global distribution of plasmaspheric hiss amplitude. The significance mainly lies in the treatment of fluctuation. The hiss amplitude can be obtained through the model simply by using  $AE^*$  and position information. The results of previous studies (Spasojevic et al., 2015, Yu J et al., 2017) show good agreement with hiss amplitude observations when for single variables ( $L$  or MLT) are considered. Since the 2D model including  $L$ /MLT or  $L$ /MLAT is of greater importance, in this study we present the fitting model to investigate the relationship between  $B_w$  and  $L$ /MLT, and also  $B_w$

and  $L$ /MLAT. Our 2D model can perform the hiss amplitude distribution by  $L$ /MLT and  $L$ /MLAT simultaneously. Beyond this, our model can be simplified for 1D usage; the results show good consistency with Spasojevic et al. (2015) and Yu J et al. (2017).

Two different methods have been implemented to separate the training group and the test group, as shown in Table 1. Our analysis indicates that Method #2, which uses the odd-number days as the training group and the even-number days as the test group, is superior in deriving well-performing fitting functions for the global hiss wave model. One possible reason can be that the training and test groups in Method #2 may reflect the phases of a solar cycle more reasonably. Several other factors that may affect the modeling results should also be considered: first, the latitudin-

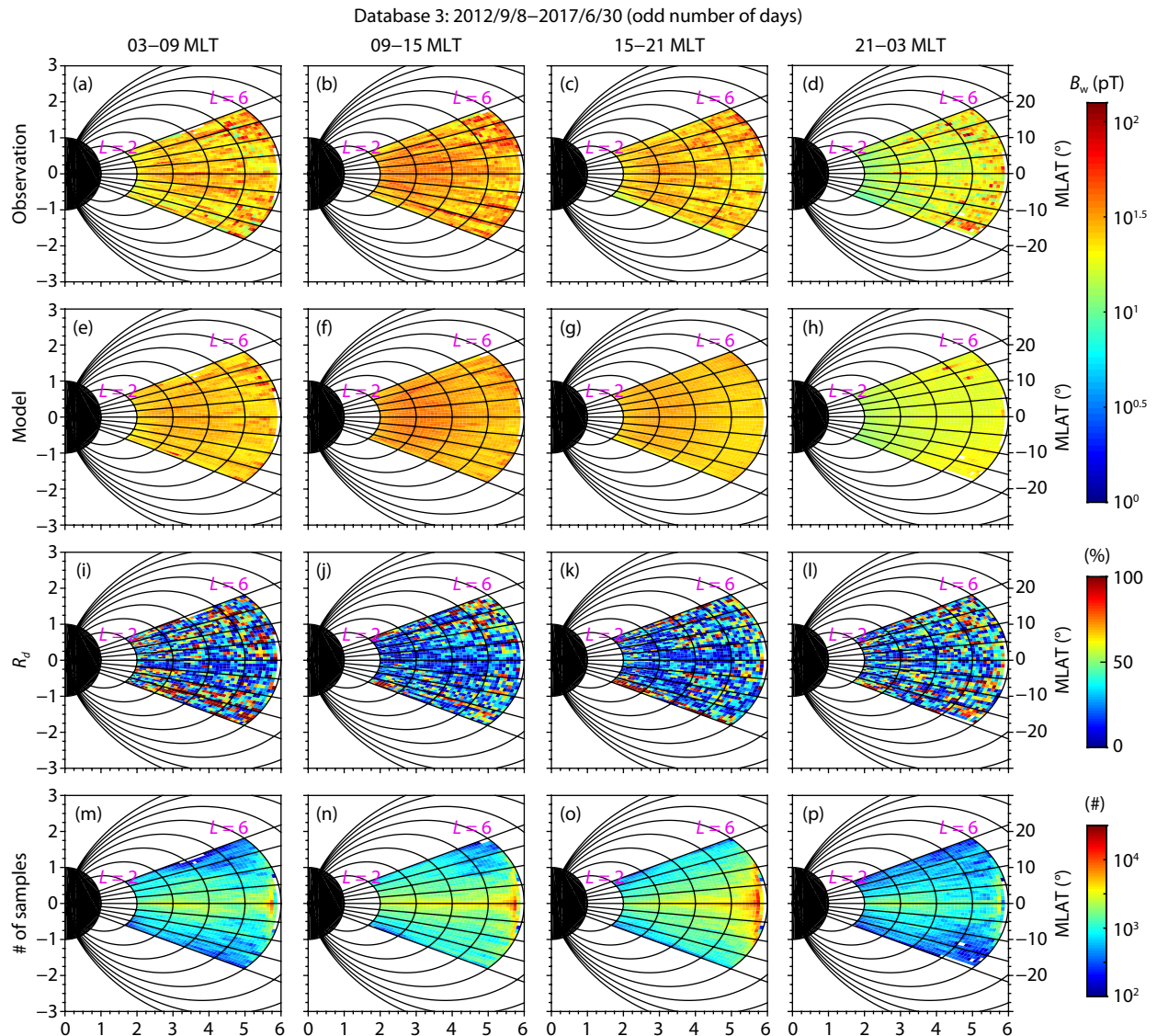


**Figure 6.** (a–d) Latitudinal  $L$ -MLAT distribution of hiss wave amplitude from observations in Database 3; (e–h) self-consistent model results of Database 3; (i–l) relative differences ( $R_d$ ) between them; (m–p) corresponding numbers of samples during different MLT sectors (left to right).

al distribution of the number of samples is dependent on the MLAT, which could be another reason why Method #1 is worse than Method #2; second, Databases 1 and 2 have more differences in the MLAT distribution, which may also be the cause of differences between the observations and model results. These unsolved questions require further investigation in future studies.

In summary, it is well demonstrated, by quantitative comparisons between the statistical observations and model results, that the empirical model in terms of fitted functions can reflect favorably the major features of the global distribution of hiss wave intensity, including the MLT asymmetry, substorm dependence, and latitudinal variations (Xiang Z et al., 2017). Because both the energy spectra and pitch angle distributions of radiation belt electrons are critically affected by hiss wave scattering (e.g., Ni BB et al., 2013, 2014, 2017, 2019; Zhao H et al., 2019; Li LY et al., 2008; Hua M et al., 2019), and because the scattering rates increase proportionally to the square of hiss amplitude for the near-resonance

cases, our results therefore provide an empirically useful analytic model to be readily used for numerical quantification of hiss-driven electron diffusion coefficients and global simulations of resultant modulation of radiation belt electron dynamics in response to varying conditions of solar wind and geomagnetic activities.

### Acknowledgments

This work was supported by the B-type Strategic Priority Program of the Chinese Academy of Sciences (Grant No. XDB41000000), the NSFC grants 41674163, 41974186, 41704162, 41904144, and 41904143, and the pre-research projects on Civil Aerospace Technologies No. D020308, D020104 and D020303 funded by China National Space Administration. We thank the Van Allen Probes EMFISIS Science Team for providing the data. The EMFISIS data are obtained from EMFISIS website (<https://emfisis.physics.uiowa.edu/data/index>); the geomagnetic activity indices are obtained from the NASA OMNIWeb (<http://cdaweb.gsfc.nasa.gov>).

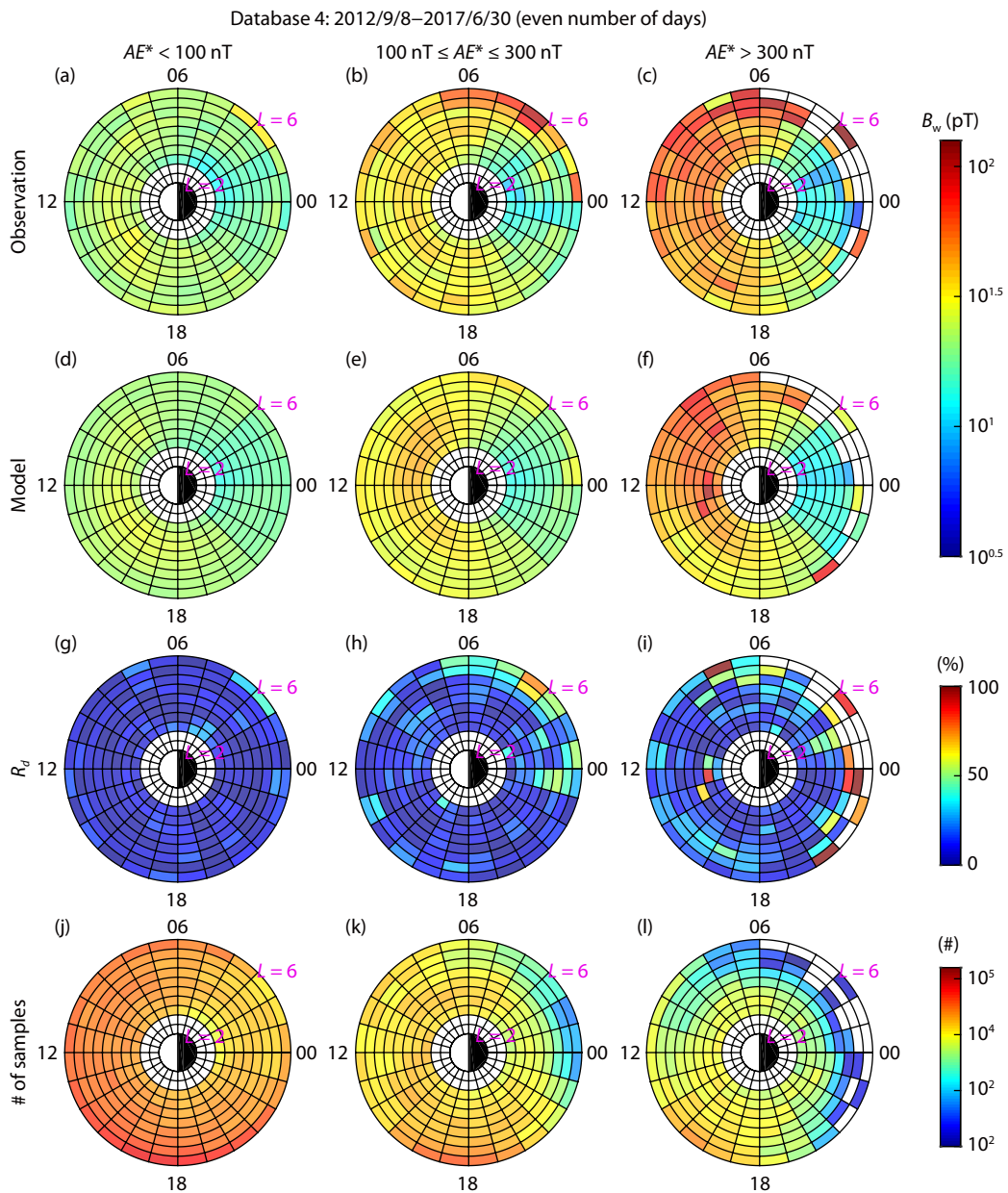


**Figure 7.** (a–c) Global  $L$ -MLT distribution of hiss wave amplitude from observations of Database 4; (d–f) model results calculated by Method #2 of Database 4; (g–i) relative differences ( $R_d$ ) between them; (j–l) Corresponding numbers of samples during quiet, moderate, and active times (left to right).

## Supplementary Materials

Fitting coefficients of global hiss wave amplitudes described by Equation (1), with  $A$ ,  $B$ ,  $C$ , and  $D$  standing for  $L/10$ ,  $\text{MLT}/24$ ,  $\text{MLAT}/20$ , and  $\text{AE}^*/500$  respectively in the tables below.

## References

- Albert, J. M. (1994). Quasi-linear pitch angle diffusion coefficients: Retaining high harmonics. *Journal of Geophysical Research*, 99(A12), 23,741–23,745. <https://doi.org/10.1029/94JA02345>
- Abel, B., and Thorne, R. M. (1998a). Electron scattering loss in Earth's inner magnetosphere: 1. dominant physical processes. *J. Geophys. Res. Space Phys.*, 103(A2), 2385–2396. <https://doi.org/10.1029/97JA02919>
- Abel, B., and Thorne, R. M. (1998b). Electron scattering loss in Earth's inner magnetosphere: 2. sensitivity to model parameters. *J. Geophys. Res. Space Phys.*, 103(A2), 2397–2407. <https://doi.org/10.1029/97JA02920>
- Agapitov, O., Artemyev, A., Krasnoselskikh, V., Khotyaintsev, Y. V., Mourenas, D., Breuillard, H., Balikhin, M., and Rolland, G. (2013). Statistics of whistler mode waves in the outer radiation belt: Cluster STAFF-SA measurements. *J. Geophys. Res. Space Phys.*, 118(6), 3407–3420. <https://doi.org/10.1002/jgra.50312>
- Agapitov, O. V., Artemyev, A. V., Mourenas, D., Kasahara, Y., and Krasnoselskikh, V. (2014). Inner belt and slot region electron lifetimes and energization rates based on AKEMONO statistics of whistler waves. *J. Geophys. Res. Space Phys.*, 119(4), 2876–2893. <https://doi.org/10.1002/2014JA019886>
- Bortnik, J., Thorne, R. M., and Meredith, N. P. (2008). The unexpected origin of plasmaspheric hiss from discrete chorus emissions. *Nature*, 452(7183), 62–66. <https://doi.org/10.1038/nature06741>
- He, F., Zhang, X. X., Chen, B., and Fok, M. C. (2011). Reconstruction of the

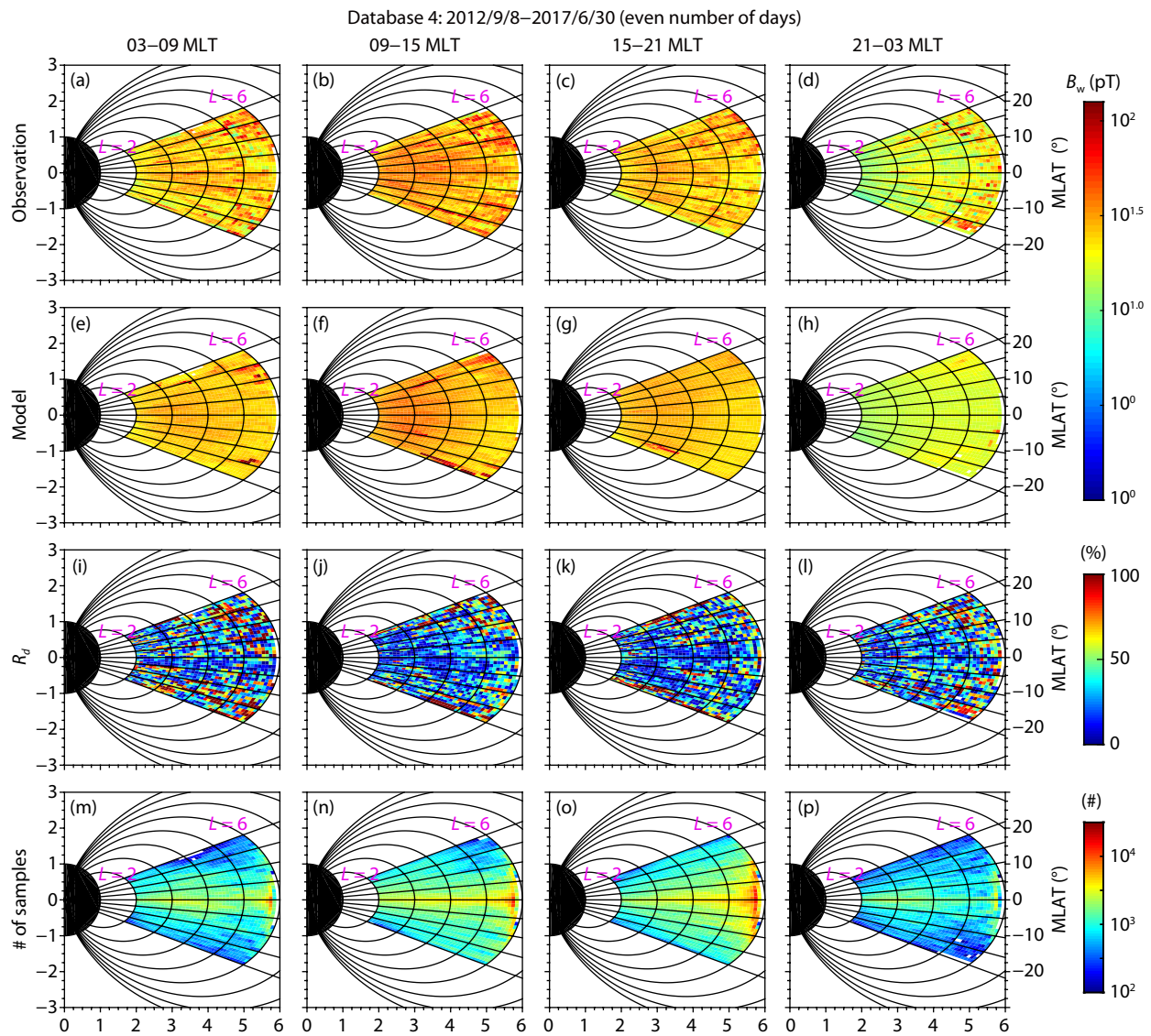


**Figure 8.** (a–d) Latitudinal  $L$ -MLAT distribution of hiss wave amplitude from observations in Database 4; (e–h) model results calculated by Method #2 of Database 4; (i–l) relative differences ( $R_d$ ) between them; (m–p) corresponding numbers of samples during different MLT sectors (left to right).

**Table S1.** For the case of  $3 \leq \text{MLT} < 9$  when  $\Delta E^* < 100 \text{ nT}$ .

	$A^3$	$A^2$	$A$	1
$B^2 C^2 D^2$	-266514.9971	396133.7612	-184520.1083	22417.0169
$B^2 C^2 D$	54078.0900	-73746.8387	34075.0324	-4159.9805
$B^2 C^2$	-5621.4548	6523.7330	-2538.6389	289.3744
$B^2 C D^2$	711003.3528	-869701.6097	336135.7473	-36131.3944
$B^2 C D$	-162514.4515	198471.9394	-77133.7749	8403.3444
$B^2 C$	5460.4956	-7038.6107	2935.1354	-339.9128
$B^2 D^2$	12383.3494	36038.8107	-26108.7679	4090.9090
$B^2 D$	-5046.8114	-11409.0749	8713.9449	-1313.8818
$B^2$	1167.8761	-144.9262	-286.1891	57.2291
$B C^2 D^2$	109462.4900	-189592.8830	95759.0780	-12030.0396

Continued from Table S1

	$A^3$	$A^2$	$A$	1
$BC^2D$	-22770.5610	35900.9413	-17996.1522	2267.7925
$BC^2$	2614.9908	-3200.3276	1298.0470	-150.7319
$BCD^2$	-399735.7029	486461.0926	-185965.6797	19759.4410
$BCD$	89648.4882	-108883.2325	41859.1725	-4512.8917
$BC$	-3072.1548	3905.0191	-1596.3226	181.6559
$BD^2$	13119.3847	-34517.3428	17091.5814	-2350.3062
$BD$	-3057.1654	10660.3297	-5661.1607	768.2433
$B$	-133.1410	-385.0074	285.6188	-41.8407
$C^2D^2$	-8925.5333	19872.9552	-11002.8916	1400.9854
$C^2D$	1961.5531	-3790.8888	2059.6952	-260.8511
$C^2$	-260.5572	337.9240	-141.9811	16.4166
$CD^2$	49165.7159	-59712.5852	22671.5047	-2376.0183
$CD$	-10827.3537	13107.7268	-4999.7083	531.5406
$C$	374.1982	-471.3872	189.8032	-21.1261
$D^2$	-3683.7443	5466.8612	-2190.9823	278.3865
$D$	1167.1453	-1918.8436	821.3382	-101.4842
1	-47.9098	104.0285	-49.1017	7.6187

**Table S2.** For  $3 \leq \text{MLT} < 9$  when  $100 \text{ nT} \leq AE^* \leq 300 \text{ nT}$ .

	$A^3$	$A^2$	$A$	1
$B^2C^2D^2$	331653.7991	-308724.7892	85439.2375	-6834.3308
$B^2C^2D$	-241950.8713	225856.0542	-63900.4468	5298.6881
$B^2C^2$	42092.5539	-39622.5307	11528.0842	-989.3248
$B^2CD^2$	-30330.8124	36914.0125	-16526.4601	2262.0703
$B^2CD$	-813.0019	-3918.5268	6060.2020	-1315.9209
$B^2C$	2057.5584	-824.1222	-811.5823	243.6292
$B^2D^2$	-137886.6057	142068.7276	-42807.3836	3577.8427
$B^2D$	106875.8033	-110329.2476	33724.7500	-2866.8768
$B^2$	-19767.3055	20493.2503	-6391.3540	555.4488
$BC^2D^2$	-186784.8467	173025.2772	-47277.7337	3707.6257
$BC^2D$	137389.8139	-127709.9661	35625.4506	-2887.3134
$BC^2$	-23877.6413	22387.1216	-6417.5656	537.2465
$BCD^2$	17663.7459	-20102.7491	8714.8459	-1168.0038
$BCD$	-1797.5484	3467.5402	-3431.5976	692.6035
$BC$	-792.7300	316.6578	415.8051	-123.0988
$BD^2$	70177.6085	-71475.3936	21189.5131	-1740.4780
$BD$	-54224.0265	55197.0739	-16574.8150	1386.2145
$B$	10003.5159	-10274.1115	3168.2252	-271.3915
$C^2D^2$	23356.0741	-21140.9820	5549.2345	-406.8674

Continued from Table S2

	$A^3$	$A^2$	$A$	1
$C^2D$	-17446.3873	15895.2195	-4271.5491	324.4526
$C^2$	3086.8747	-2847.3167	790.1641	-62.5019
$CD^2$	-1941.2948	2015.7225	-843.7662	110.3938
$CD$	311.1382	-340.1256	319.5751	-65.1887
$C$	74.4323	-51.4628	-31.4615	11.3554
$D^2$	-7709.1922	7698.6539	-2219.8704	175.7890
$D$	6041.5387	-6004.5814	1750.7038	-141.2786
1	-1111.2043	1114.1224	-333.5586	29.1836

**Table S3.** For  $3 \leq \text{MLT} < 9$  when  $AE^* > 300$  nT.

	$A^3$	$A^2$	$A$	1
$B^2C^2D^2$	6132.7613	-27930.8705	11651.5562	-1113.2363
$B^2C^2D$	-42815.7524	82673.4313	-30777.2382	2865.2209
$B^2C^2$	37990.7017	-55785.8343	19486.3362	-1779.3551
$B^2CD^2$	-64036.0325	51549.2193	-12378.0540	847.4860
$B^2CD$	114298.9448	-90899.8767	21070.5138	-1340.9157
$B^2C$	-45958.2849	35709.9717	-7758.8220	413.6833
$B^2D^2$	16006.5829	-7613.0548	801.5318	6.6229
$B^2D$	-28049.8313	11604.8521	-500.9973	-103.9934
$B^2$	7399.3240	132.7468	-1469.2754	195.2219
$BC^2D^2$	7989.1234	7255.6867	-4462.3906	465.6041
$BC^2D$	3203.5654	-30890.6393	13397.9060	-1306.4381
$BC^2$	-12601.4592	24661.2024	-9224.4162	861.4047
$BCD^2$	34438.2147	-26848.3917	6264.1346	-419.9600
$BCD$	-59565.2802	45655.6805	-10175.6042	623.2360
$BC$	22997.2083	-16977.2613	3429.1713	-161.0901
$BD^2$	-11028.8682	5649.5698	-775.4366	22.5878
$BD$	19404.6519	-8840.1046	820.2465	14.5789
$B$	-5664.8571	820.0595	630.4501	-92.2497
$C^2D^2$	-3547.9859	880.4892	148.3611	-28.8548
$C^2D$	4192.7312	584.0480	-909.5064	107.4561
$C^2$	-350.2315	-1663.0556	808.4976	-81.9262
$CD^2$	-4156.7722	3070.2755	-688.0119	44.8482
$CD$	6954.1099	-5030.6860	1065.6385	-62.0595
$C$	-2606.0522	1792.1408	-330.7502	12.9542
$D^2$	1830.1727	-989.6628	157.7775	-7.3790
$D$	-3320.6072	1671.6640	-226.6916	7.6697
1	1146.7147	-400.4969	-6.6888	7.2731

**Table S4.** For  $9 \leq \text{MLT} < 15$  when  $\text{AE}^* < 100$  nT.

	$A^3$	$A^2$	$A$	1
$B^2C^2D^2$	629884.9981	-704561.3756	236123.6731	-24458.1348
$B^2C^2D$	-186449.5938	214143.2284	-73522.9196	7600.7679
$B^2C^2$	9859.9713	-12173.5796	4461.3441	-472.1497
$B^2CD^2$	40426.9278	-74824.5923	27475.3091	-1057.7387
$B^2CD$	26081.4585	-22956.4169	7566.3318	-1206.4892
$B^2C$	-3150.9226	3150.7331	-1054.2248	130.7475
$B^2D^2$	-425735.9035	445985.9123	-137474.9455	12161.9005
$B^2D$	102505.6268	-109727.0210	34662.5765	-3156.3718
$B^2$	-4963.7051	5566.8348	-1842.3759	172.6923
$BC^2D^2$	-578928.5758	643869.6617	-215185.3916	22565.6035
$BC^2D$	171190.6501	-197223.3796	68048.7862	-7118.7784
$BC^2$	-9095.0724	11370.7693	-4215.4383	450.4360
$BCD^2$	-53180.7345	88403.4235	-32210.0716	1505.6013
$BCD$	-25102.6522	21531.6270	-6873.9905	1130.0184
$BC$	3372.6792	-3349.1747	1098.5430	-133.1092
$BD^2$	445754.0520	-469938.1203	146202.9813	-13142.2304
$BD$	-105703.5663	114052.7380	-36428.4483	3371.1101
$B$	5136.6792	-5815.8431	1949.8871	-185.6119
$C^2D^2$	128119.2472	-140783.7539	46586.5678	-4936.3869
$C^2D$	-37662.4911	43430.8074	-15013.9783	1586.4379
$C^2$	1998.3167	-2533.6223	950.2927	-102.4939
$CD^2$	16734.6294	-25521.5664	9214.2985	-499.8170
$CD$	5836.5497	-4845.1243	1480.8104	-252.5459
$C$	-883.7282	870.9973	-279.6956	32.9784
$D^2$	-114081.9787	120791.1982	-37827.7391	3439.3908
$D$	26693.0495	-28982.9744	9339.3403	-873.6237
1	-1282.2221	1458.1511	-491.7567	48.6827

**Table S5.** For  $9 \leq \text{MLT} < 15$  when  $100 \text{ nT} \leq \text{AE}^* \leq 300 \text{ nT}$ .

	$A^3$	$A^2$	$A$	1
$B^2C^2D^2$	-169864.1685	147455.0384	-32886.8818	1505.1670
$B^2C^2D$	130383.1144	-112560.8228	24526.2227	-962.8418
$B^2C^2$	-22365.0240	19117.4984	-3981.7294	114.3034
$B^2CD^2$	-139011.8288	145722.3046	-48273.5030	4794.3010
$B^2CD$	115734.3602	-122340.2537	40873.8247	-4056.8831
$B^2C$	-21231.0770	22556.7890	-7555.3091	740.8990
$B^2D^2$	-37444.2493	48027.6866	-18563.9424	1952.8074
$B^2D$	26352.4851	-34065.8492	13311.0788	-1439.8912
$B^2$	-4917.4746	6152.4054	-2368.9573	257.3706

Continued from Table S5

	$A^3$	$A^2$	$A$	1
$BC^2D^2$	193321.4523	-174237.8943	42071.8227	-2420.7938
$BC^2D$	-148952.9454	133411.3280	-31560.3969	1655.2613
$BC^2$	25620.7880	-22754.5790	5203.0059	-233.4869
$BCD^2$	143821.9669	-149879.9036	49306.6154	-4866.6454
$BCD$	-119807.0605	125903.8889	-41793.2646	4125.1234
$BC$	22021.6420	-23271.2594	7751.7619	-756.4568
$BD^2$	35237.0632	-45609.4155	17734.8507	-1864.9925
$BD$	-24541.1752	32148.4689	-12680.9205	1373.0821
$B$	4612.8304	-5824.8700	2259.7143	-245.7838
$C^2D^2$	-53549.9666	49738.0385	-12707.6404	829.3473
$C^2D$	41574.0809	-38362.6236	9630.8017	-590.3443
$C^2$	-7201.5844	6603.9642	-1618.0443	90.3080
$CD^2$	-36699.1157	37931.4620	-12344.1107	1204.9972
$CD$	30593.7282	-31889.1734	10479.5269	-1023.9428
$C$	-5641.7512	5917.5459	-1953.9292	188.9122
$D^2$	-7846.7149	10377.5080	-4099.8631	433.1066
$D$	5360.0358	-7230.9882	2914.8373	-317.1766
1	-980.3300	1267.2780	-501.2689	56.7315

**Table S6.** For  $9 \leq \text{MLT} < 15$  when  $AE^* > 300$  nT.

	$A^3$	$A^2$	$A$	1
$B^2C^2D^2$	-31993.8136	36350.2045	-12567.1004	1153.6804
$B^2C^2D$	65046.8285	-76045.8471	26740.9094	-2483.7590
$B^2C^2$	-29375.6610	35116.2003	-12477.5683	1147.1708
$B^2CD^2$	-150.4137	-931.4761	888.6293	-135.8866
$B^2CD$	17481.1852	-15612.7851	3539.6859	-188.5353
$B^2C$	-15577.0949	14709.2991	-3816.5509	263.8378
$B^2D^2$	1501.7008	-2734.6008	1196.6681	-122.1471
$B^2D$	-5178.1268	8533.7132	-3533.0662	353.4630
$B^2$	3170.0384	-5116.3017	2086.0565	-209.4092
$BC^2D^2$	32561.2017	-37073.5770	12812.5938	-1176.8440
$BC^2D$	-65390.7075	76840.6779	-27080.6938	2522.4960
$BC^2$	28769.8107	-34819.4777	12474.0677	-1155.9478
$BCD^2$	-775.3958	2061.5781	-1276.5211	171.4736
$BCD$	-15580.0601	13246.3806	-2720.2183	111.5433
$BC$	14743.2103	-13635.5241	3438.1251	-227.0693
$BD^2$	-1534.6187	2744.9817	-1183.0081	119.6319
$BD$	5378.4352	-8676.4002	3526.4529	-348.9818
$B$	-3102.6496	5018.5670	-2032.9596	202.7243
$C^2D^2$	-8149.1462	9285.7846	-3200.7904	293.8390

Continued from Table S6

	$A^3$	$A^2$	$A$	1
$C^2D$	16073.3979	-18981.3168	6694.7619	-624.9779
$C^2$	-6818.1265	8377.6824	-3026.2587	282.4056
$CD^2$	472.4027	-830.8122	420.3314	-51.8246
$CD$	3289.2412	-2608.3565	448.6455	-6.4834
$C$	-3397.5641	3064.5458	-743.7383	45.6803
$D^2$	411.2663	-703.0306	293.8160	-29.3386
$D$	-1452.1749	2246.5070	-885.0933	86.5118
1	830.0756	-1301.6374	516.5562	-49.1952

**Table S7.** For  $15 \leq \text{MLT} < 21$  when  $AE^* < 100$  nT.

	$A^3$	$A^2$	$A$	1
$B^2C^2D^2$	502956.9265	-539128.3919	162997.4350	-11347.8250
$B^2C^2D$	-113445.6282	119077.1007	-34329.3681	2265.3844
$B^2C^2$	3276.0336	-3230.7921	770.7469	-29.5738
$B^2CD^2$	157210.5677	-213224.4394	81353.1972	-9973.3017
$B^2CD$	-74359.6575	94332.0713	-34624.8291	3840.0784
$B^2C$	4960.6349	-6373.8833	2359.7361	-255.2794
$B^2D^2$	-325638.9011	359494.1791	-115501.3005	9258.6430
$B^2D$	51615.4180	-56416.3949	17634.4180	-1328.2824
$B^2$	-573.9870	603.2576	-145.7251	-1.0749
$BC^2D^2$	-718212.2574	771041.5231	-233097.7411	16232.2811
$BC^2D$	159873.2797	-168175.6795	48398.1224	-3172.3739
$BC^2$	-4424.4420	4377.1854	-1025.1029	35.5277
$BCD^2$	-164889.3781	237262.1277	-93580.3798	12233.4214
$BCD$	97030.0976	-124752.9570	46246.4867	-5224.7885
$BC$	-6799.8377	8825.3793	-3292.1941	359.7621
$BD^2$	494266.5954	-545293.6129	175472.2080	-14174.7311
$BD$	-79249.9878	86620.8634	-27190.6987	2080.3337
$B$	971.3968	-1018.7705	257.5490	-3.1859
$C^2D^2$	262395.7950	-282540.0548	85653.9028	-6033.4447
$C^2D$	-57857.2535	61113.1883	-17628.2573	1163.2656
$C^2$	1576.1757	-1571.5676	367.7632	-12.7950
$CD^2$	36477.0645	-59567.5142	24948.3281	-3593.2854
$CD$	-30929.8153	40537.0913	-15224.6182	1756.3501
$C$	2308.0058	-3034.7736	1142.4299	-126.1022
$D^2$	-189357.3284	208806.6558	-67321.9007	5486.7131
$D$	31157.3121	-34050.0090	10738.0056	-835.8921
1	-441.6704	456.7027	-118.3040	4.9437

**Table S8.** For  $15 \leq \text{MLT} < 21$  when  $100 \text{ nT} \leq AE^* \leq 300 \text{ nT}$ .

	$A^3$	$A^2$	$A$	1
$B^2C^2D^2$	93608.8811	-99129.7690	34001.2091	-4022.7276
$B^2C^2D$	-76919.5127	83277.6117	-28706.9010	3299.9839
$B^2C^2$	12047.6256	-13441.2021	4741.1544	-554.2596
$B^2CD^2$	-101043.1854	108320.6616	-34647.3669	3143.5469
$B^2CD$	88592.0627	-95344.3339	30571.9557	-2754.5159
$B^2C$	-15301.5783	16315.5162	-5164.9895	448.3235
$B^2D^2$	-90468.5901	102938.6861	-35797.5100	3751.9817
$B^2D$	72443.6599	-81900.6731	28201.0568	-2915.3123
$B^2$	-12884.7832	14594.5450	-5019.4980	512.0447
$BC^2D^2$	-131111.6890	138410.6585	-47580.7641	5719.2727
$BC^2D$	107716.9153	-116697.5797	40429.3929	-4720.5602
$BC^2$	-16725.0565	18755.6724	-6678.4186	796.3718
$BCD^2$	160921.7848	-173343.3489	55671.2223	-5053.0726
$BCD$	-140460.4094	151887.3397	-48922.0289	4420.9577
$BC$	24425.4249	-26222.1361	8360.2948	-732.0562
$BD^2$	134092.0390	-153291.3326	53557.2123	-5635.3154
$BD$	-108035.3083	122651.0370	-42407.2877	4399.2731
$B$	19075.0580	-21693.7179	7491.9321	-768.7761
$C^2D^2$	45135.6942	-47371.0058	16302.6130	-1992.7369
$C^2D$	-37088.5944	40149.0026	-13979.0482	1659.5441
$C^2$	5691.3770	-6414.5665	2309.8626	-281.7614
$CD^2$	-62815.8241	67885.5183	-21856.3421	1983.0585
$CD$	54705.6403	-59355.6320	19176.0729	-1736.4545
$C$	-9583.8709	10341.7678	-3314.4556	292.2754
$D^2$	-49409.4172	56695.8478	-19880.8569	2097.0375
$D$	40032.1588	-45603.7988	15819.2237	-1644.4106
1	-6979.0670	7962.5121	-2758.1727	286.2224

**Table S9.** For  $15 \leq \text{MLT} < 21$  when  $AE^* > 300 \text{ nT}$ .

	$A^3$	$A^2$	$A$	1
$B^2C^2D^2$	-1829.3591	-587.4156	1164.1513	-259.9248
$B^2C^2D$	-1757.2425	4277.4628	-3162.8914	686.3738
$B^2C^2$	-3003.5657	3324.1760	-371.8121	-184.5379
$B^2CD^2$	-12211.0051	10877.9200	-2708.4724	203.9189
$B^2CD$	34058.6401	-32021.0297	8632.3466	-686.0533
$B^2C$	-15231.1783	14413.9471	-3857.5838	297.3967
$B^2D^2$	4236.7924	-3758.4586	941.0589	-45.7887
$B^2D$	-6926.4342	6521.6285	-1678.5517	61.2233
$B^2$	2985.1491	-3203.8975	910.2741	-37.0109

Continued from Table S9

	$A^3$	$A^2$	$A$	1
$BC^2D^2$	700.9561	2672.3186	-2260.9915	430.0345
$BC^2D$	5060.9111	-8754.0784	5522.8809	-1092.7459
$BC^2$	3854.3675	-4227.9542	245.1139	304.1879
$BCD^2$	17249.2805	-15189.3713	3705.5840	-272.1701
$BCD$	-48633.6842	45430.6074	-12127.1988	952.8634
$BC$	21845.9720	-20534.2901	5436.1308	-413.5728
$BD^2$	-5921.7142	5368.5874	-1374.5254	69.1577
$BD$	10043.8037	-9731.4713	2574.3572	-104.3332
$B$	-4786.1755	5257.6537	-1535.5133	73.1924
$C^2D^2$	224.8326	-1408.1570	963.8340	-169.6245
$C^2D$	-2273.1720	3649.4858	-2214.6980	420.1827
$C^2$	-1467.1437	1555.0067	-47.5418	-117.9417
$CD^2$	-6012.4862	5221.5247	-1241.6993	88.5275
$CD$	17125.1575	-15871.8048	4184.9588	-324.8277
$C$	-7718.2414	7195.9406	-1879.5879	141.0361
$D^2$	2083.5260	-1928.0878	503.1514	-26.1625
$D$	-3685.4162	3651.8279	-984.5011	43.4187
1	1962.9860	-2184.9943	650.9175	-33.2332

**Table S10.** For  $21 \leq \text{MLT} < 3$  when  $AE^* < 100$  nT.

	$A^3$	$A^2$	$A$	1
$B^2C^2D^2$	78763.3201	-70953.4215	17898.7742	-1439.3581
$B^2C^2D$	-21308.5777	19385.5327	-4916.1973	371.5218
$B^2C^2$	1355.2223	-1248.0642	324.4378	-24.3469
$B^2CD^2$	-81512.5192	86332.2005	-26434.5405	2334.6949
$B^2CD$	20283.1122	-21191.7675	6459.3212	-575.1379
$B^2C$	-1352.0203	1402.9724	-429.5032	38.8220
$B^2D^2$	-44623.4589	53791.7013	-20025.8662	2291.6462
$B^2D$	14313.1686	-16487.0934	5830.2838	-636.0968
$B^2$	-1096.0362	1209.4196	-405.8388	41.1090
$BC^2D^2$	-77283.1734	68446.0694	-16839.1821	1364.0079
$BC^2D$	21090.8216	-18943.0997	4712.5379	-358.0203
$BC^2$	-1362.0066	1246.7419	-321.9076	24.5684
$BCD^2$	91013.8294	-97245.0751	30272.9614	-2722.3949
$BCD$	-22484.0807	23802.3541	-7400.8736	671.8152
$BC$	1478.9923	-1556.7355	485.3099	-44.5170
$BD^2$	46269.0705	-55171.8689	20368.9337	-2334.2277
$BD$	-14739.9411	16875.8488	-5941.3381	649.9034
$B$	1126.6437	-1242.7771	417.5811	-42.5079
$C^2D^2$	3222.2702	-2493.1073	584.5990	-79.1772

Continued from Table S10

	$A^3$	$A^2$	$A$	1
$C^2D$	-1104.8296	964.6767	-251.1849	27.5374
$C^2$	75.8759	-68.7066	18.7087	-1.9568
$CD^2$	-10859.7647	12081.3927	-4078.3578	401.0778
$CD$	2518.3306	-2831.8652	970.0610	-97.1894
$C$	-147.7759	165.3412	-56.4296	5.6820
$D^2$	-1896.6714	2283.9892	-893.5652	119.4325
$D$	677.7034	-764.1779	272.3790	-33.1051
1	-51.6867	54.9470	-17.4602	3.2163

**Table S11.** For  $21 \leq \text{MLT} < 3$  when  $100 \text{ nT} \leq AE^* \leq 300 \text{ nT}$ .

	$A^3$	$A^2$	$A$	1
$B^2C^2D^2$	-57019.3361	43046.7962	-10082.0642	734.2537
$B^2C^2D$	26850.9381	-18283.2664	3771.4534	-233.2010
$B^2C^2$	-2572.1777	1423.4839	-204.7980	4.6060
$B^2CD^2$	-28576.4602	23138.1742	-5344.0995	331.6583
$B^2CD$	23254.2636	-19765.9681	4821.6157	-324.0250
$B^2C$	-4627.3395	4144.7511	-1084.7928	81.1160
$B^2D^2$	-3724.8879	5266.9111	-1561.2734	101.8974
$B^2D$	6397.9463	-7117.0772	1984.8604	-136.5674
$B^2$	-1655.9537	1735.3889	-481.9074	33.9444
$BC^2D^2$	54049.7630	-40590.7766	9461.8151	-686.6623
$BC^2D$	-25582.3355	17266.6460	-3531.5461	216.7897
$BC^2$	2466.9510	-1341.9042	187.9051	-3.8626
$BCD^2$	29740.3530	-24332.8418	5690.6267	-357.2131
$BCD$	-24353.1457	20852.1989	-5133.2978	347.5365
$BC$	4808.6367	-4323.6752	1136.2007	-85.0516
$BD^2$	4602.6476	-6209.6000	1885.5551	-136.1870
$BD$	-6905.4185	7690.0970	-2191.3714	159.2823
$B$	1729.1972	-1824.6403	515.9028	-37.7617
$C^2D^2$	-3648.1521	3017.1415	-795.8842	67.5684
$C^2D$	2072.6618	-1645.7120	424.8206	-36.4804
$C^2$	-268.1996	209.5025	-54.8183	4.9326
$CD^2$	-4172.9902	3801.8255	-1057.3326	87.1069
$CD$	3148.4384	-2908.2295	818.6345	-68.2110
$C$	-521.9749	489.1567	-139.7461	11.8942
$D^2$	140.1179	-8.3992	-14.1078	1.1023
$D$	54.9715	-134.5670	46.2524	-3.3622
1	-39.8132	51.6017	-15.2822	2.5156

**Table S12.** For  $21 \leq \text{MLT} < 3$  when  $AE^* > 300$  nT.

	$A^3$	$A^2$	$A$	1
$B^2C^2D^2$	-4767.3972	2391.6324	-186.9034	-13.7966
$B^2C^2D$	8849.6518	-3612.6320	-73.7785	71.8434
$B^2C^2$	-3941.6253	1194.0994	218.7614	-49.3895
$B^2CD^2$	-237.0725	120.0989	-38.6316	2.3034
$B^2CD$	-1389.1577	1306.8915	-298.5480	21.8833
$B^2C$	1803.1691	-1589.1820	386.2908	-28.9243
$B^2D^2$	-2120.6692	1732.8122	-434.2252	33.8314
$B^2D$	4825.2319	-4080.9516	1061.9505	-85.3927
$B^2$	-2359.9272	2116.9879	-582.8724	47.8042
$BC^2D^2$	4009.2050	-1790.6478	39.7558	24.5674
$BC^2D$	-7322.6675	2447.2619	347.6579	-91.0338
$BC^2$	3323.3825	-761.7557	-309.4931	54.8654
$BCD^2$	29.1433	-12.5949	30.9978	-3.0094
$BCD$	1803.2254	-1493.6573	299.5264	-18.8906
$BC$	-2002.5882	1667.8647	-381.6669	26.9726
$BD^2$	2285.5556	-1890.1988	478.2440	-37.4343
$BD$	-5197.1076	4430.9076	-1158.6021	93.2198
$B$	2535.1290	-2279.0977	627.2383	-51.3663
$C^2D^2$	76.2616	-136.5977	51.8708	-4.7539
$C^2D$	-163.8528	276.4589	-101.8775	9.0071
$C^2$	-25.5844	-36.2580	19.3630	-1.5412
$CD^2$	-117.7559	131.5090	-44.7731	4.1161
$CD$	248.3031	-299.9492	106.9029	-10.2377
$C$	-57.1891	106.1994	-45.2434	4.7107
$D^2$	-192.7063	172.2809	-44.3984	3.3900
$D$	475.4294	-421.9168	108.1886	-8.2028
1	-241.3631	214.4019	-54.5530	5.2218

- plasmasphere from Moon-based EUV images. *J. Geophys. Res. Space Phys.*, 116(A11), A11203. <https://doi.org/10.1029/2010JA016364>
- He, F., Zhang, X. X., Chen, B., Fok, M. C., and Zou, Y. L. (2013). Moon-based EUV imaging of the Earth's plasmasphere: Model simulations. *J. Geophys. Res. Space Phys.*, 118(11), 7085–7103. <https://doi.org/10.1002/2013JA018962>
- He, F., Zhang, X. X., Chen, B., Fok, M. C., and Nakano, S. (2016). Determination of the Earth's plasmapause location from the CE-3 EUVC images. *J. Geophys. Res. Space Phys.*, 121(1), 296–304. <https://doi.org/10.1002/2015JA021863>
- He, F., Zhang, X. X., Lin, R. L., Fok, M. C., Katus, R. M., Liemohn, M. W., Gallagher, D. L., and Nakano, S. (2017). A new solar wind-driven global dynamic plasmapause model: 2. Model and validation. *J. Geophys. Res. Space Phys.*, 122(7), 7172–7187. <https://doi.org/10.1002/2017JA023913>
- Hua, M., Ni, B. B., Li, W., Gu, X. D., Fu, S., Shi, R., Xiang, Z., Cao, X., Zhang, W. X., and Guo, Y. J. (2019). Evolution of radiation belt electron pitch angle distribution due to combined scattering by plasmaspheric hiss and magnetosonic waves. *Geophys. Res. Lett.*, 46(6), 3033–3042. <https://doi.org/10.1029/2018GL081828>
- Katus, R. M., Gallagher, D. L., Liemohn, M. W., Keesee, A. M., and Sarno-Smith, L. K. (2015). Statistical storm time examination of MLT-dependent plasmapause location derived from IMAGE EUV. *J. Geophys. Res. Space Phys.*, 120(7), 5545–5559. <https://doi.org/10.1002/2015JA021225>
- Kim, K. C., Lee, D. Y., and Shprits, Y. (2015). Dependence of plasmaspheric hiss on solar wind parameters and geomagnetic activity and modeling of its global distribution. *J. Geophys. Res. Space Phys.*, 120(2), 1153–1167. <https://doi.org/10.1002/2014JA020687>
- Kletzing, C. A., Kurth, W. S., Acuna, M., MacDowall, R. J., Torbert, R. B., Averkamp, T., Bodet, D., Bounds, S. R., Chutter, M., ... Tyler, J. (2013). The electric and magnetic field instrument suite and integrated science (EMFISIS) on RBSP. *Space Sci. Rev.*, 179(1–4), 127–181. <https://doi.org/10.1007/s11214-013-9993-6>
- Li, L. Y., Cao, J. B., and Zhou, G. C. (2008). Whistler-mode waves modify the high-energy electron slot region and the outer radiation belt. *Chinese J. Geophys. (in Chinese)*, 51(2), 316–324. <https://doi.org/10.3321/j.issn:0001-5733.2008.02.004>
- Li, W., Thorne, R. M., Bortnik, J., Reeves, G. D., Kletzing, C. A., Kurth, W. S., Hospodarsky, G. B., Spence, H. E., Blake, J. B., ... Thaller, S. A. (2013). An

- unusual enhancement of low-frequency plasmaspheric hiss in the outer plasmasphere associated with substorm-injected electrons. *Geophys. Res. Lett.*, 40(15), 3798–3803. <https://doi.org/10.1002/grl.50787>
- Li, W., Chen, L., Bortnik, J., Thorne, R. M., Angelopoulos, V., Kletzing, C. A., Kurth, W. S., and Hospodarsky, G. B. (2015a). First evidence for chorus at a large geocentric distance as a source of plasmaspheric hiss: Coordinated THEMIS and Van Allen Probes observation. *Geophys. Res. Lett.*, 42(2), 241–248. <https://doi.org/10.1002/2014GL062832>
- Li, W., Ma, Q., Thorne, R. M., Bortnik, J., Kletzing, C. A., Kurth, W. S., Hospodarsky, G. B., and Nishimura, Y. (2015b). Statistical properties of plasmaspheric hiss derived from Van Allen Probes data and their effects on radiation belt electron dynamics. *J. Geophys. Res. Space Phys.*, 120(5), 3393–3405. <https://doi.org/10.1002/2015JA021048>
- Lyons, L. R., Thorne, R. M., and Kennel, C. F. (1972). Pitch-angle diffusion of radiation belt electrons within the plasmasphere. *J. Geophys. Res.*, 77(19), 3455–3474. <https://doi.org/10.1029/JA077i019p03455>
- Lyons, L. R., and Thorne, R. M. (1973). Equilibrium structure of radiation belt electrons. *J. Geophys. Res.*, 78(13), 2142–2149. <https://doi.org/10.1029/JA078i013p02142>
- Meredith, N. P., Horne, R. B., Thorne, R. M., Summers, D., and Anderson, R. R. (2004). Substorm dependence of plasmaspheric hiss. *J. Geophys. Res. Space Phys.*, 109(A6), A06209. <https://doi.org/10.1029/2004JA010387>
- Meredith, N. P., Horne, R. B., Cliver, M. A., Horsfall, D., Thorne, R. M., and Anderson, R. R. (2006a). Origins of plasmaspheric hiss. *J. Geophys. Res. Space Phys.*, 111(A9), A09217. <https://doi.org/10.1029/2006JA011707>
- Meredith, N. P., Horne, R. B., Glauert, S. A., Thorne, R. M., Summers, D., Albert, J. M., and Anderson, R. R. (2006b). Energetic outer zone electron loss timescales during low geomagnetic activity. *J. Geophys. Res. Space Phys.*, 111(A5), A05212. <https://doi.org/10.1029/2005JA011516>
- Meredith, N. P., Horne, R. B., Glauert, S. A., and Anderson, R. R. (2007). Slot region electron loss timescales due to plasmaspheric hiss and lightning-generated whistlers. *J. Geophys. Res. Space Phys.*, 112(A8), A08214. <https://doi.org/10.1029/2007JA012413>
- Mosier, S. R., Kaiser, M. L., and Brown, L. W. (1973). Observations of noise bands associated with the upper hybrid resonance by the IMP 6 radio astronomy experiment. *J. Geophys. Res.*, 78(10), 1673–1679. <https://doi.org/10.1029/JA078i010p01673>
- Ni, B. B., Bortnik, J., Thorne, R. M., Ma, Q. L., and Chen, L. J. (2013). Resonant scattering and resultant pitch angle evolution of relativistic electrons by plasmaspheric hiss. *J. Geophys. Res. Space Phys.*, 118(12), 7740–7751. <https://doi.org/10.1002/2013JA019260>
- Ni, B. B., Li, W., Thorne, R. M., Bortnik, J., Ma, Q. L., Chen, L. J., Kletzing, C. A., Kurth, W. S., Hospodarsky, G. B., ... Claudepierre, S. G. (2014). Resonant scattering of energetic electrons by unusual low-frequency hiss. *Geophys. Res. Lett.*, 41(6), 1854–1861. <https://doi.org/10.1002/2014GL059389>
- Ni, B. B., Hua, M., Zhou, R. X., Yi, J., and Fu, S. (2017). Competition between outer zone electron scattering by plasmaspheric hiss and magnetosonic waves. *Geophys. Res. Lett.*, 44(8), 3465–3474. <https://doi.org/10.1002/2017GL072989>
- Ni, B. B., Huang, H., Zhang, W. X., Gu, X. D., Zhao, H., Li, X. L., Baker, D., Fu, S., Xiang, Z., and Cao, X. (2019). Parametric sensitivity of the formation of reversed electron energy spectrum caused by plasmaspheric hiss. *Geophys. Res. Lett.*, 46(8), 4134–4143. <https://doi.org/10.1029/2019gl082032>
- Orlova, K., Spasojevic, M., and Shprits, Y. (2014). Activity-dependent global model of electron loss inside the plasmasphere. *Geophys. Res. Lett.*, 41(11), 3744–3751. <https://doi.org/10.1002/2014GL060100>
- Santolík, O., Parrot, M., Storey, L. R. O., Pickett, J. S., and Gurnett, D. A. (2001). Propagation analysis of plasmaspheric hiss using Polar PWI measurements. *Geophys. Res. Lett.*, 28(6), 1127–1130. <https://doi.org/10.1029/2000GL012239>
- Shi, R., Li, W., Ma, Q. L., Reeves, G. D., Kletzing, C. A., Kurth, W. S., Hospodarsky, G. B., Spence, H. E., Blake, J. B., ... Claudepierre, S. G. (2017). Systematic evaluation of low-frequency hiss and energetic electron injections. *J. Geophys. Res. Space Phys.*, 122(10), 10263–10274. <https://doi.org/10.1002/2017JA024571>
- Smith, E. J., Frandsen, A. M. A., Tsurutani, B. T., Thorne, R. M., and Chan, K. W. (1974). Plasmaspheric hiss intensity variations during magnetic storms. *J. Geophys. Res.*, 79(16), 2507–2510. <https://doi.org/10.1029/JA079i016p02507>
- Spasojevic, M., Shprits, Y. Y., and Orlova, K. (2015). Global empirical models of plasmaspheric hiss using Van Allen Probes. *J. Geophys. Res. Space Phys.*, 120(12), 10370–10383. <https://doi.org/10.1002/2015JA021803>
- Summers, D., Ni, B. B., and Meredith, N. P. (2007a). Timescales for radiation belt electron acceleration and loss due to resonant wave-particle interactions: 1. Theory. *J. Geophys. Res. Space Phys.*, 112(A4), A04206. <https://doi.org/10.1029/2006JA011801>
- Summers, D., Ni, B. B., and Meredith, N. P. (2007b). Timescales for radiation belt electron acceleration and loss due to resonant wave-particle interactions: 2. Evaluation for VLF chorus, ELF hiss, and electromagnetic ion cyclotron waves. *J. Geophys. Res. Space Phys.*, 112(A4), A04207. <https://doi.org/10.1029/2006JA011993>
- Thorne, R. M., Smith, E. J., Burton, R. K., and Holzer, R. E. (1973). Plasmaspheric hiss. *J. Geophys. Res. Space Phys.*, 78(10), 1581–1596. <https://doi.org/10.1029/JA078i010p01581>
- Thorne, R. M., Smith, E. J., Fiske, K. J., and Church, S. R. (1974). Intensity variation of ELF hiss and chorus during isolated substorms. *Geophys. Res. Lett.*, 1(5), 193–196. <https://doi.org/10.1029/GL001i005p00193>
- Thorne, R. M., Church, S. R., and Gorney, D. J. (1979). On the origin of plasmaspheric hiss: The importance of wave propagation and the plasmapause. *J. Geophys. Res. Space Phys.*, 84(A9), 5241–5247. <https://doi.org/10.1029/JA084iA09p05241>
- Tsurutani, B. T., Falkowski, B. J., Pickett, J. S., Santolík, O., and Lakhina, G. S. (2015). Plasmaspheric hiss properties: Observations from Polar. *J. Geophys. Res. Space Phys.*, 120(1), 414–431. <https://doi.org/10.1002/2014JA020518>
- Verbanac, G., Pierrard, V., Bandić, M., Darrouzet, F., Rauch, J. L., and Décréau, P. (2015). The relationship between plasmapause, solar wind and geomagnetic activity between 2007 and 2011. *Ann. Geophys.*, 33(10), 1271–1283. <https://doi.org/10.5194/angeo-33-1271-2015>
- Xiang, Z., Tan, J. Q., Ni, B. B., Gu, X. D., Cao, X., Zou, Z. Y., Zhou, C., Fu, S., Shi, R., ... Wang, H. (2017). A statistical analysis of the global distribution of plasmaspheric hiss based on Van Allen Probes wave observations. *Acta Phys. Sin. (in Chinese)*, 66(3), 039401. <https://doi.org/10.7498/aps.66.039401>
- Yu, J., Li, L. Y., Cao, J. B., Chen, L., Wang, J., and Yang, J. (2017). Propagation characteristics of plasmaspheric hiss: Van Allen Probe observations and global empirical models. *J. Geophys. Res. Space Phys.*, 122(4), 4156–4167. <https://doi.org/10.1002/2016JA023372>
- Zhang, X. X., He, F., Lin, R. L., Fok, M. C., Katus, R. M., Liemohn, M. W., Gallagher, D. L., and Nakano, S. (2017a). A new solar wind-driven global dynamic plasmapause model: 1. Database and statistics. *J. Geophys. Res. Space Phys.*, 122(7), 7153–7171. <https://doi.org/10.1002/2017JA023912>
- Zhang, X. X., He, F., Chen, B., Shen, C., and Wang, H. N. (2017b). Correlations between plasmapause evolutions and auroral signatures during substorms observed by Chang'e-3 EUV Camera. *Earth Planet. Phys.*, 1(1), 35–43. <https://doi.org/10.26464/epp2017005>
- Zhao, H., Ni, B., Li, X., Baker, D. N., Johnston, W. R., Zhang, W., Xiang, Z., Gu, X., Jaynes, A. N., ... Boyd, A. J. (2019). Plasmaspheric hiss waves generate a reversed energy spectrum of radiation belt electrons. *Nat. Phys.*, 15(4), 367–372. <https://doi.org/10.1038/s41567-018-0391-6>